Monitoring Aromatic Picosecond to Nanosecond Dynamics in Proteins via ^{13}C Relaxation: Expanding Perturbation Mapping of the Rigidifying Core Mutation, V54A, in Eglin c[†]

Joshua A. Boyer[‡] and Andrew L. Lee*[,‡,§]

Department of Biochemistry and Biophysics, School of Medicine, and Division of Medicinal Chemistry and Natural Products, School of Pharmacy, University of North Carolina, Chapel Hill, North Carolina 27599

Received November 26, 2007; Revised Manuscript Received February 5, 2008

ABSTRACT: Long-range effects, such as allostery, have evolved in proteins as a means of regulating function via communication between distal sites. An NMR-based perturbation mapping approach was used to more completely probe the dynamic response of the core mutation V54A in the protein eglin c by monitoring changes in picosecond to nanosecond aromatic side-chain dynamics and H/D exchange stabilities. Previous side-chain dynamics studies on this mutant were limited to methyl-bearing residues, most of which were found to rigidify on the picosecond to nanosecond time scale in the form of a contiguous "network". Here, high precision ^{13}C relaxation data from 13 aromatic side chains were acquired by applying canonical relaxation experiments to a newly developed carbon labeling scheme [Teilum et al. (2006) *J. Am. Chem. Soc. 128*, 2506–2507]. The fitting of model-free parameters yielded S^2 variability which is intermediate with respect to backbone and methyl-bearing side-chain variability and τ_e values that are approximately 1 ns. Inclusion of the aromatic dynamic response results in an expanded network of dynamically coupled residues, with some aromatics showing increases in flexibility, which partially offsets the rigidification in methyl side chains. Using amide hydrogen exchange, dynamic propagation on a slower time scale was probed in response to the V54A perturbation. Surprisingly, regional stabilization (slowed exchange) 10–12 Å from the site of mutation was observed despite a global destabilization of 1.5 kcal·mol^{-1}. Furthermore, this unlikely pocket of stabilized residues colocalizes with increases in aromatic flexibility on the faster time scale. Because the converse is also true (destabilized residues colocalize with rigidification on the fast time scale), a plausible entropy-driven mechanism is discussed for relating colocalization of opposing dynamic trends on vastly different time scales.

Motional flexibility, or dynamics, is essential for protein stability and function (*2–6*). Recently, native state protein dynamics have been thought to be crucial for mediating allosteric signaling or, stated more generally, long-range communication (*7–14*). One of the major challenges is the experimental characterization of dynamic processes relevant to intramolecular signal transduction. Toward this goal, NMR[1] spectroscopy is uniquely suited to noninvasively characterize both structure and dynamics in a site-specific manner. Mapping flexibility by NMR is therefore an important application for understanding signaling in proteins. It is desirable to characterize dynamic networks with high resolution, in terms of spatial coverage through the use of a large number of probes and in terms of temporal coverage sensitivity to different time scales. Here, a previously determined dynamic network in eglin c is expanded through use of ^{13}C relaxation in aromatic side chains and amide hydrogen exchange.

In previous work, the globular protein eglin c was used as a model for characterizing dynamic and structural responses to mutation (*10, 15*). Pathways of dynamic changes (in response to mutation) were evident even in this simple protein, with the majority of responses observed in picosecond to nanosecond side-chain fluctuations, as monitored by relaxation effects. Although the approach used was general in principle, only methyl-bearing side chains were probed using ^2H spin relaxation. This methodology applied to the V54A mutant of eglin c yielded an apparent dynamic network of excited responders on the picosecond to nanosecond time scale. The result was the bulk rigidification of select contiguous methyl-bearing residues radiating out from the site of mutation to the periphery of the protein's structured regions. Although such a generalized rigidification might be

[†] This research was supported by NIH Grant GM066009.

* To whom correspondence should be addressed. E-mail: drewlee@unc.edu. Phone: (919) 966-7821. Fax: (919) 843-5150.

[‡] Department of Biochemistry and Biophysics, School of Medicine, University of North Carolina.

[§] Division of Medicinal Chemistry and Natural Products, School of Pharmacy, University of North Carolina.

[1] Abbreviations: NMR, nuclear magnetic resonance; HX, hydrogen exchange; T_1, spin–lattice relaxation time constant; T_2, spin–spin relaxation time constant; NOE, nuclear Overhauser effect; CSA, chemical shift anisotropy; S^2, Lipari−Szabo "model-free" generalized order parameter; S^2_{axis}, axial model-free order parameter for methyl groups; τ_e, Lipari−Szabo model-free effective correlation time; R_{ex}, Lipari−Szabo model-free chemical exchange term; τ_m, correlation time for overall tumbling; HSQC, heteronuclear single-quantum coherence; ΔG_U, free energy change associated with two-state unfolding events; GdnHCl, guanidine hydrochloride; ΔG_{HX}, local free energy change determined via HX.

10.1021/bi702330t CCC: $40.75
Published on Web 04/05/2008

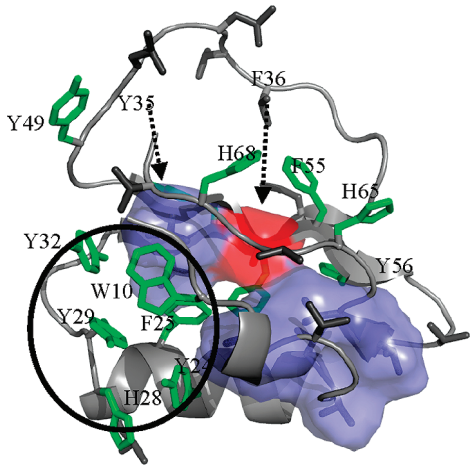

FIGURE 1: Reporters and responders of eglin c. The methyl-bearing residues that respond to the V54A mutation in eglin c are shown as a contiguous slate surface (*15*). The site of mutation is shown in red. Those methyl residues that were unobservable or exhibit no change are shown in gray. The "new" aromatic reporters are shown in green. The circled region is the "aromatic corner" which completes the hydrophobic core of the protein and was inaccessible in previous studies. The dashed arrows indicate residues in the back of the structure as orientated. Figures in this paper were rendered in PyMol (www.pymol.org) using a *Rosetta Design* (*62*) modeled V54A* structure based on the X-ray structure of eglin c (1CSE) (*70*).

reflected in the globally measured heat capacity (*15*), this was found not to be the case (*16*). One possibility to describe this scenario is the limited spatial distribution of methyl-bearing residues. Eglin c contains a substantial number of aromatic residues (39% of the 36 hydrophobic side-chain reporters), many of which are contained in an "aromatic corner" (Figure 1), a region that was underrepresented on the picosecond to nanosecond time scale. In an effort to more thoroughly sample the effects of mutation on dynamics and energy transmission in proteins, we have sought more probes to report on these changes. Recently, a convenient method for appropriate ^{13}C labeling into aromatic groups for relaxation studies was introduced (*1*). Here, in an effort to more comprehensively characterize the dynamics in the eglin c dynamic network, we show that this labeling scheme is effective for characterizing picosecond to nanosecond dynamics of nearly all aromatic side chains, yielding data that are well fit by model-free dynamics parameters.

Aromatic residues are important probes because of their locations in hydrophobic cores and binding interfaces (*17–20*). Until recently, accessing picosecond to nanosecond information in regard to these aromatic residues has been complicated by neighboring ^{13}C ring nuclei. To circumvent these effects, natural abundance studies (*21*) and unique isotopic-labeling schemes (*22*) have been applied to this problem in regard to relaxation. Here, we utilize a new labeling scheme developed by Teilum et al. (*1*) to acquire data from aromatic probes on the picosecond to nanosecond time scale. The labeling scheme eliminates the occurrence of adjacent ^{13}C neighbors, allowing the $^{13}C-^{1}H$ dipole–dipole interaction to dominate the relaxation mechanism (*23*). The ^{13}C relaxation data are well fit to Lipari−Szabo model-free spectral densities (*24, 25*), indicating dominant motions on the time scale of approximately 1 ns. Although the application of techniques utilized in this paper is well-suited for characterizing picosecond to nanosecond dynamics of aromatic groups in proteins in general, it should be particularly useful in aromatic-rich binding interfaces.

Relaxation experiments and native hydrogen exchange have proven to be useful for mapping perturbation responses and identifying participating elements of putative networks (*10, 13, 26–30*), as they both can serve as local measures of conformational flexibility. To supplement the picosecond to nanosecond time scale provided by spin relaxation studies, and more thoroughly examine the changes in flexibility upon mutation from a temporal aspect, we used hydrogen exchange (HX) to characterize a much slower time scale. The labile nature of the amide proton−nitrogen bond results in an exchange phenomenon that can yield information on motions that occur on the millisecond to hour time scale (*31*). When an amide participates in a hydrogen bond, the rate of exchange is dependent upon the rate of "opening" fluctuations. EX2 exchange behavior occurs when the rate of closing (or refolding) is much faster than the rate of intrinsic exchange, enabling the calculation of the equilibrium between an opening event and an exchange event. The determination of equilibrium constants between the native state and all other states can provide local free energies (*32, 33*). Although these measurements are thermodynamic and not kinetic in nature, HX-determined local free energies are sensitive metrics of the dynamic fluctuations that enable exchange.

Through monitoring aromatic picosecond to nanosecond motions and hydrogen exchange to report on millisecond to hour motions, we have more thoroughly characterized the dynamic response of the V54A mutation both spatially and temporally. Combined with previously published results on the methyl-bearing side chains, information of the picosecond to nanosecond time regime is more heterogeneous, both spatially and in the nature of response. The collective picosecond to nanosecond motions are now seen to become more flexible as well as more rigid. Upon measuring the changes in local free energies upon mutation characterized by hydrogen exchange, surprisingly, a region of eglin c distal to the site of the globally destabilizing mutation (V54A) shows an *increase* in local stabilities (slowed exchange), whereas the local measurements of the core are more consistent with the global measurements. The results provide a more complete picture of mutational perturbation and its consequences on multiple time scales. Interestingly, the superimposition of the changes on two measurements shows a colocalization of destabilization and rigidification as well as stabilization and an increase in flexibility, a phenomenon in need of further investigation.

EXPERIMENTAL PROCEDURES

Expression and Purification. WT* eglin c (* indicating F10W mutation) and a variant containing further mutation V54A were expressed in *Escherichia coli* BL21(DE3) cells in media containing 99% [1-^{13}C]glucose as the sole carbon source as described by Teilum et al. (*1*). Aromatic assignment experiments required samples grown in [U-^{13}C]-D-glucose (99%) and $^{15}NH_4Cl$ (99%). Samples used for hydrogen exchange were grown in M9 media containing $^{15}NH_4Cl$ (99%). Purification was completed as previously described (*10, 15*). All NMR samples contained 2.0 mM eglin c in our standard

buffer (20 mM KPO_4, 50 mM KCl, 0.02% NaN_3, and 10% D_2O, pH 7.0).

NMR Spectroscopy. NMR data were collected on 500 and 600 MHz Varian INOVA spectrometers equipped with triple-resonance probes at 37 °C (temperature calibrated with ethylene glycol) with the exception of the HX studies at 25 °C (calibrated with methanol). Spectra were processed using NMRPipe (*34*) and analyzed with the aid of NMRView (*35*). Aromatic assignments of WT and V54A eglin c samples were made on uniformly labeled samples containing ^{15}N and ^{13}C via (HB)CB(CGCD)HD and (HB)CB(CGCDCE)HE experiments (*36*).

^{13}C Relaxation. ^{13}C relaxation data were collected on samples isotopically labeled using the method of Teilum et al. (*1*) at both spectrometer fields using standard T_1, T_2, and NOE relaxation experiments of Farrow et al. (*37*) modified for ^{13}C using an INEPT delay consistent with a one-bond $^1H-^{13}C$ *J*-coupling of 154 Hz. ^{13}C T_1 data were collected with relaxation delays of 35, 95, 175, 270, 375, 490, 620, 755, and 905 ms at 500 MHz and with delays of 30, 85, 150,230, 320, 420, 525, 645, and 770 at 600 MHz. ^{13}C CPMG based T_2 data were collected with relaxation delays of 4.5, 9, 13.5, 22.5, 36.1, 54.2, 72.2, 94.8, and 126.4 ms at both fields, with spacing between 180° pulses of 534 μs. Uncertainties for all peak intensities were assessed using duplicate points (underlined delays above). Peak intensities were extracted using NMRView and fitted to single-exponential decays using a Levenberg–Marquardt algorithm. $\{^1H\}-^{13}C$ NOE data at both fields were collected with a ^1H saturation period of 3.0 s and uncertainties assessed from root mean squared base-plane noise. The six ^{13}C relaxation data sets were fitted to the model-free formalism utilizing relxn2.2 and the front end interface rvi (*10*), with a CH bond length of 1.101 Å (*38*) and a CSA value of 170 ppm (*21, 22*). The model fits showed a heightened sensitivity to precise NOE values due to the shallow parameter space. The fits were performed with isotropic tumbling times of $\tau_m = 4.62$ ns for WT (*10*) and 4.64 ns for V54A (*15*), in accordance with the rotational correlation times determined for the backbone ^{15}N data of the respective proteins. To include the sole tryptophan residue, previously acquired ^{15}N relaxation data (*15*) for the indole of W10 were analyzed and fit to the model-free formalism using a CSA value of –89 ppm (*39*).

Model Selection. Model selection using the standard five model-free models (S^2; S^2 and τ_e; S^2 and R_{ex}; S^2, τ_e, and R_{ex}; S^2_s,S^2_f, and τ_s) was performed using the model-selection subroutine of rvi (*10*). Briefly, the subroutine fits each of the model-free models to each residue, calculating the Akaike's information criteria (AIC) (*40*) of each model. The model with the lowest AIC value was selected. Model selection is described in more depth in the Results section.

Hydrogen Exchange. Uniformly ^{15}N-labeled proteins were passed through spin columns containing Sephadex G25 equilibrated with 90% D_2O, 20 mM KPO_4, 55 mM KCl, 0.02% NaN_3, and $pD_{corrected}$ 7.0. Samples were quickly placed in an NMR tube and transferred into the spectrometer. HX data were recorded at 25 °C for consistency with global stability measurements. Initially, a series of $^1H-^{15}N$ SOFAST HMQC (*41*) spectra was acquired with a single plane acquisition requiring approximately 20 s, followed by $^1H-^{15}N$ HSQC pseudo-3D spectra acquired with a single plane acquisition requiring approximately 6.5 min. Time points were collected for 48 h. Peak intensity error was calculated from rms base-plane noise for each plane. Peak intensities were extracted from each plane and fit to a simple three-parameter monoexponential. Given EX2 behavior, the exchange rates (k_{ex}) and Molday factors (*32, 33*) were used to calculate the local free energies and propagated errors.

Stopped-Flow Fluorescence Kinetic Studies. To ensure EX2 behavior, folding rates of WT and V54A were approximated by triangulating ΔG_U, the midpoint of the equilibrium folding transition, with the folding and unfolding rates at two concentrations of GdnHCl at 25 °C (see below). These rates were monitored on a SPEX Fluorolog-3 research T-format spectrofluorometer with stopped-flow housing, F-3009 MicroFlow. Ten micromolar protein solutions at native and denaturing conditions were mixed 1:1 to a final sample volume of ~32 μL. Fluorescence of the tryptophan probe was excited at 295 nm, and emission counts were monitored at 350 nm with a path length of 2 mm and instrument dead time of 5 ms. The DATAMAX software package was used to export intensity vs time data. Rates were fit using Kaleidagraph (Synergy Software) and simple three-parameter exponential rise and decay functions. To assess EX2 exchange, approximate folding and unfolding rates were estimated from a reduced set of kinetic measurements using the procedure described below. Refolding studies were done at final GdnHCl concentrations of 2.25 and 1.6 M for WT and V54A, respectively; the folding rates at these concentrations were determined to be 2.8 s^{-1} (WT) and 1.6 s^{-1} (V54A). Similarly, unfolding studies were performed at final GdnHCl concentrations of 4.5 M for WT and 4 M for V54A, giving rates of 0.4 s^{-1} and 0.8 s^{-1}, respectively. If one considers a chevron plot, the two *y*-intercepts are the projected rates of folding and unfolding in the absence of denaturant, and the intersection of the projected lines is the midpoint of the folding transition. Because of eglin c's apparent two-state folding mechanism (*42, 43*), it can be reasonably assumed that the kinetic midpoint of folding and the kinetic ΔG_{H_2O} are similar to those determined through equilibrium studies. We can define the line that travels through the midpoint (x_3, y_3) and the measured point in folding conditions (x_1, y_1) with the function:

$$f(x) = \frac{y_3 - y_1}{x_3 - x_1}(x) + \ln(k_f) \quad (1)$$

Similarly, we can define the line that travels through the midpoint (x_3, y_3) and the measured point in unfolding conditions (x_2, y_2) with the function:

$$g(x) = \frac{y_3 - y_2}{x_3 - x_2}(x) + \ln(k_u) \quad (2)$$

Evaluating at the midpoint (x_3, y_3), the functions become

$$y_3 = \frac{y_3 - y_1}{x_3 - x_1}(x_3) + \ln(k_f) \quad (3a)$$

and

$$y_3 = \frac{y_3 - y_2}{x_3 - x_2}(x_3) + \ln(k_u) \quad (3b)$$

Equating the right-hand side of each equation, and rearrangement, gives

$$\frac{y_3 - y_1}{x_3 - x_1}(x_3) - \frac{y_3 - y_2}{x_3 - x_2}(x_3) = \frac{\Delta G}{RT} \quad (4)$$

leaving an expression where all values are known, save y_3. After solving for y_3, the rates (k_u and k_f) can be back-calculated.

Contingency Table and Fisher Exact Test. The Fisher exact test uses a hypergeometric function to determine the *p*-values of rare tables, defined as those having individual *p*-values less than the cutoff *p*-value of the given contingency table (*44, 45*). The sum of the rare *p*-values provides the *p*-value which serves as the basis to accept or reject the null hypothesis. Using SAS version 9.1.3 (SAS Institute, Cary, NC) the *p*-value of the contingency table (see Discussion) was determined to be $p = 0.0246$.

RESULTS

To probe the motions of aromatic side chains, ^{13}C relaxation experiments were carried out on eglin c expressed with the labeling scheme of Teilum et al. (*1*). This scheme introduces ^{13}C into the δ carbons of phenylalanine and tyrosine aromatic rings, the $\delta 2$ and $\epsilon 1$ carbons of histidine rings, and the $\delta 1$ and $\epsilon 3$ carbons of tryptophan rings (*1*). The picosecond to nanosecond motions of the aromatic side chains were characterized using ^{13}C relaxation measurements at two fields (a total of six measurements), followed by fitting to model-free parameters (*24, 25*). Specific models (standard model-free spectral density functions 1–5) were selected via AIC statistical protocols (*40*). This method enabled the addition of 13 reporters to a previous study of the effect of the V54A mutation on picosecond to nanosecond dynamics (*15*).

Aromatic ^{13}C Relaxation. Precise relaxation measurements are important for robust fitting of model-free parameters. For WT eglin c, the average ^{13}C T_1 values were 0.31 and 0.37 s at 500 and 600 ^1H MHz, respectively, with typical standard error in individual T_1 values of 1.2% and 1.1%. The average ^{13}C T_2 values were 0.049 and 0.046 s at 500 and 600 ^1H MHz with an average error of 1.5% and 1.6%. The average $\{^1H\}-^{13}C$ NOE enhancement values were 1.2 at both fields (the positive sign of carbon's gyromagnetic ratio yields an enhancement greater than 1) with equivalent average errors of 1.4%. Although the high precision of these data results in slightly elevated χ^2 values when fitting the model-free parameters, overall the ^{13}C aromatic relaxation data were robustly fit using the model-free formalism. It should be noted that, for model-free fitting, high precision (<3% error) in the ^{13}C NOE is important for robust determination of parameters, particularly when the effective correlation time (τ_e, τ_s) is longer than ~500 ps. This was confirmed with simulated data and subsequent fitting to model-free models 2 and 5 (data not shown). This was found to be more of a problem for ^{13}C data than for ^{15}N data and is therefore due to the different Larmor frequencies contributing to relaxation. This sensitivity requirement is alleviated by the inherently greater sensitivity of ^{13}C over ^{15}N.

An Entire Ring Order Parameter. Unlike previous ^{13}C labeling schemes found in the literature (*22, 46*), carbons at both δ positions of phenylalanine and tyrosine residues are labeled.

These positions are in exchange and lead to single peaks in the $^1H-^{13}C$ HSQC spectrum arising from both $C^{\delta}-H^{\delta}$ spin pairs. Thus, the T_1, T_2, and NOE measurements of the phenylalanine and tyrosine residues acquired here are assumed to report on the average effect experienced at each site. It is, however, possible that shift degeneracy (in both ^1H and ^{13}C) exists for the $\delta 1$ and $\delta 2$ positions, for which slow flipping would not be identified by simple inspection. This scenario would result either in (1) biexponential relaxation or (2) similar relaxation behavior that, upon analysis, would afford effective averaging of the two sites. For these reasons, due to ring geometry, the order parameters reported here for these residues can be considered a generalized order parameter for the entire aromatic ring. It should also be mentioned that ring flips on a time scale commensurate with overall tumbling (or faster) would serve to reduce the order parameter and would be indistinguishable from other nonflip ring motions. For packed aromatic rings, we view this as unlikely, though this possibility should not be ignored. Our interpretation is supported by mining of an existing 80 ns molecular dynamics simulation of eglin c (*47*), which showed that the order parameter of $C^{\delta 1}-H^{\delta 1}$ bond vectors correlates with the order parameter of corresponding $C^{\delta 2}-H^{\delta 2}$ vectors with an R^2 value of 0.9942. Also, order parameters of $C^{\delta 1}-H^{\delta 1}$ bond vectors correlate with corresponding $C^{\epsilon 2}-H^{\epsilon 2}$ vectors (and vice versa $C^{\delta 2}-H^{\delta 2}$ vs $C^{\epsilon 1}-H^{\epsilon 1}$) with an R^2 value of 0.9936. No ring flipping occurred throughout the course of the entire simulation, with the exception of Y35 and Y49. These two residues are highly solvent exposed, and their low order parameters (Figure 2) may indicate significant contribution from symmetric ring flipping.

Table 1: Selection of Model-Free Parameters[a]

residue	model (WT)	model (V54A)
W10 ($^{15}N^{\epsilon 1}-^1H$)	4	5
Y24	2	5
F25	5	5
H28 ($^{13}C^{\delta 2}-^1H$)	4	4
Y29	2	2
Y32	5	5
Y35	5	5
F36	5	5
Y49	5	5
F55	5	5
Y56	2	2
H65 ($^{13}C^{\delta 2}-^1H$)	4	2
H68 ($^{13}C^{\delta 2}-^1H$)	4	4

[a] Model 1, S^2; model 2, S^2, τ_e; model 3, S^2, R_{ex}; model 4, S^2, τ_e, R_{ex}; model 5, S^2_f, S^2_s, τ_s.

Aromatic Model-Free Parameters. The fitted aromatic model-free parameters for WT and V54A are shown in Figure 2. The order parameters are either S^2 (model 2) or $S^2_{combined}$ (model 5), where $S^2_{combined}$ is equal to the product of S^2_s and S^2_f. Perhaps unsurprisingly, the measured order parameters (Figure 2A) show a greater range (0.35–0.89) than those displayed by the backbone and a smaller range than those displayed by methyl groups (*15*). Interestingly, the $\tau_{e/s}$'s (Figure 2B) reported by the fitting of the tyrosine and phenylalanine residues are on the order of 500–1500 ps, independent of the model selected. These $\tau_{e/s}$ values are an order of magnitude greater than those reported by ^{15}N backbone studies (~50 ps) (*15*), again supporting the notion that the measured aromatic relaxation parameters report on the picosecond to nanosecond motions of the entire, relatively rigid ring rather than a single bond vector. One general

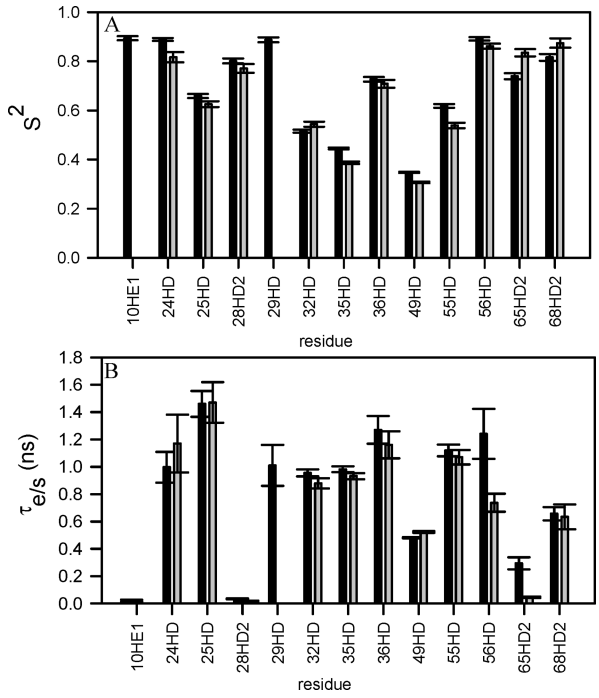

FIGURE 2: Model-free parameters for aromatic side chains. (A) Combined order parameters $S^2_{combined}$ ($S^2_{combined} = S^2$ or $S^2_s \times S^2_f$) are plotted for each aromatic side chain. An S^2 order parameter value of 1 corresponds to a completely rigid entity while an S^2 value of zero implies isotropic sampling of all possible orientations. (B) The internal correlation time constant $\tau_{e/s}$, in nanoseconds, is plotted. Black bars indicate WT values, and gray bars indicate V54A values. Error bars indicate standard errors, obtained from Monte Carlo simulations.

concern is the possible violation of the decoupling approximation of the Lipari−Szabo model-free formalism, in which the slower motion of tumbling is assumed to be independent of the internal motions of the bond vectors. Ideally, the $\tau_{e/s}$ values would be 10-fold less than the global tumbling time, τ_m ($\tau_e/\tau_m < 10$). Larger τ_e/τ_m values can introduce a bias on the determined values for S^2. However, most of the aromatic groups in eglin c are significantly buried and thus may not experience the biasing "cage" effects (*48*). In addition, simulations with noise show that ^{13}C relaxation data generated using standard model-free spectral densities can be correctly fitted by Lipari−Szabo parameters using τ_e/τ_m values observed here. Furthermore, if present, any biasing is likely to be similar between variants, which will not affect the analysis of perturbation upon mutation.

The model-free models selected for each residue are shown in Table 1. For WT, model 2 (S^2 and τ_e) was selected for residues Y24, Y29, and Y56. However, the majority of the remaining tyrosines and phenylalanines fit best to model 5 parameters, S^2_s, S^2_f, and τ_s. In the V54A variant, the same models were maintained with the exception of Y24, which fit more robustly to model 5 in the mutant. Histidine residues H28 and H68 were fitted using model 4 parameters S^2, τ_e, and R_{ex} in both mutant and wild type. H65 was fit to models 2 and 4 in the mutant and wild type, respectively. For both WT and mutant, no models lacking a τ_e (or τ_s) term were selected. As a further internal control, phenylalanine and tyrosine residues that were selected as model 2 in both variant and WT were used to verify the chemical shift anisotropy used in this analysis by fitting this parameter along with

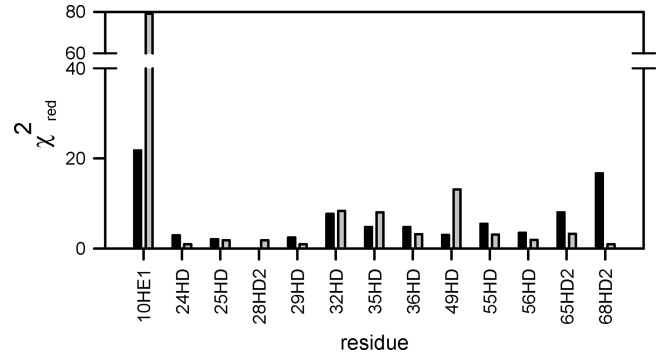

FIGURE 3: Reduced chi-square [$\chi^2_{red} = \chi^2$/degrees of freedom (where degrees of freedom = number of data points − number of fitted parameters − 1)] values from model-free fits. χ^2_{red} values for individual fits of the model-free parameters to ^{13}C relaxation data are plotted for the 13 aromatic side chains. χ^2_{red} values were determined by comparing experimental T_1, T_2, and {^1H}−^{13}C NOE data to back-calculated values. Residue W10 shows a poor fit in V54A; therefore, we place little confidence in the value fit for this residue.

model-free parameters, S^2 and τ_e. The fitted value for the combined four residues (Y24, Y29, and Y56 in WT and Y56 in V54A) was 169.6 ± 8.3 ppm compared to the 170.0 ppm used in this study, showing consistency with previously measured values (*21, 22*) and the τ_m values used here. From these results we conclude that the majority of aromatic groups undergo significant motions on the intermediate time scale of approximately 1 ns.

For most residues the model-free formalism fit the ^{13}C relaxation data well; however, some residues proved problematic. Residue F3 could not be reliably fit in either WT or V54A, most likely due to complex motions of the unstructured N-terminus. Regarding residue Y29 of the mutant, model 2 was selected, but the Monte Carlo simulations used to determine error for this residue did not converge and led to nonsensical error values. This residue may be experiencing motions unable to be fit by the model-free formalism. Also, data from bond vectors involving the histidine's $C^{\epsilon 1}$ and tryptophan's $C^{\epsilon 3}$ and $C^{\delta 1}$ displayed erratic behavior in both the T_1 and T_2 experiments. The one-bond coupling constant for these residues differs from those of the phenylalanine and tyrosine residues (for which the experiments were optimized) and thus are not included in this analysis. Figure 3 shows χ^2_{red} values for the selected model-free models fitted to the two-field relaxation data. Initially, Y35 in WT and W10 and Y49 in V54A showed large χ^2 values, providing lower confidence in the fitted parameter values for these residues. When examined further, the error for the parameters and the subsequent six relaxation measurements were unusually small. The error for these measurements was increased to 1.5% of the measured value, resulting in minimal changes in the fit parameters and an increase in error, consequently lowering the fit chi-square values. Finally, the histidine $C^{\delta 2}$−$H^{\delta 2}$ S^2 and τ_e values are questionable due to uncertainty in the appropriateness of the CSA term applied (170 ppm).

Comparison of the Aromatic Reporters of V54A and WT. While the V54A mutation results in rigidification of all responding methyl side chains (*15*), the aromatic response is more heterogeneous. Comparison of the WT and mutant V54A indicates that there are significant changes among the aromatic reporters (blue in Figure 4). In applying the criteria

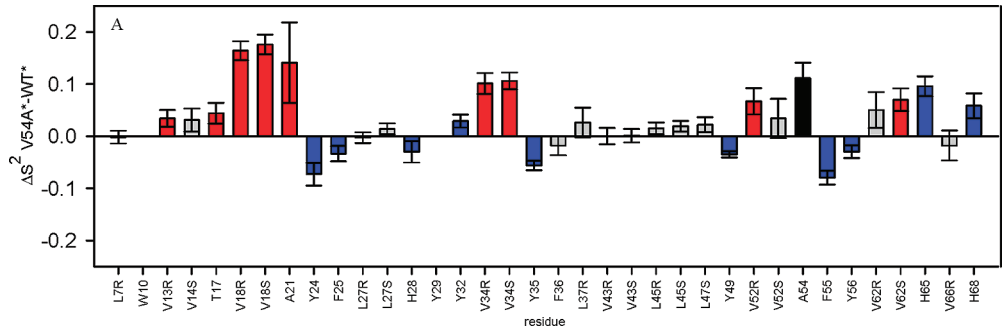

FIGURE 4: Changes in picosecond to nanosecond model-free order parameters. (A) Changes in S^2 (or S^2_{axis}) upon V54A mutation. Changes shown in red are those methyl-bearing residues reported as significant by Clarkson et al. Black denotes the site of mutation. Changes highlighted in blue are aromatic residues that display significant change. Error bars indicate propagated standard error.

for significant changes in dynamics defined previously (*10, 15*) as twice the standard error, residues Y24, F25, Y32, Y35, Y49, F55, and Y56 show significant changes in S^2; though the changes in residues 25, 32, and 56 are small (as seen in Figure 4), a significant τ_e change was seen in residue 56 (Figure 2B) . Also, residue W10 ($^{15}N^{\epsilon 1}$) showed significant change; however, fits of the mutant result in large χ^2 and hence lowered confidence in the significance of the change seen in this residue. Histidine residues 28, 65, and 68 also showed significant changes, with H28 showing a gain in flexibility, whereas H65 and H68 show increases in S^2 and significant changes in $\tau_{e/s}$.

Hydrogen Exchange. Hydrogen exchange (HX) was measured to provide additional information on flexibility in eglin c. By the method described in the Experimental Procedures section, the approximated refolding rate is 400 s^{-1} for WT and is 100 s^{-1} for V54A. Because the greatest intrinsic rate of exchange ($k_{intr,V62}$ = 14.4 s^{-1}) is nearly an order of magnitude less than our estimated folding rates and a linear dependence of exchange rate on pH was observed (data not shown), we conclude that these proteins exhibit EX2 behavior under experimental conditions (25 °C and pH 7). The exchange of amide protons with deuterium was monitored for both WT and V54A from approximately 2 min after exchange into D_2O for 48 or 24 h, respectively. In conjunction with Molday factors, the fitted exchange rates were used to determine local free energies (*32, 33*) (Figure 5A,B). Duplicate experiments have shown these local free energies to be reproducible within error (determined as described in Experimental Procedures). The discrepancy apparent in Figure 5 between globally measured stabilities (horizontal line) monitored via fluorescence and the local stabilities measured via HX (bars) is possibly due to superprotection (*49*) generated by the presence of an intermediate or residual structure in the unfolded state. Although there appears to be some evidence for residual structure in the denatured state (*50*), and eglin c shows two-state behavior in global stability measurements, further experiments will be required to provide strong evidence for either one of these possibilities.

The site-specific free energies were then compared between variant (V54A) and reference state (WT). V54A is destabilizing by 1.5 kcal·mol^{-1} according to global measurements (*10*). Residues 16, 21, 35, 54, 56, and 63 show $\Delta\Delta G_{HX}$ changes that agree well with the $\Delta\Delta G_U$ determined by fluorescence-monitored GdnHCl melts (Figure 5C), identifying these residues as reporting on global unfolding (*51*). These same amides are packed into the protein core, consistent with a global-unfolding exchange mechanism. By contrast, the local stabilities of residues 17, 20, 23, 26, 27, 29, and 32 actually increase in the variant, with those of residues 26, 27, and 29 being particularly significant. These residues are exchanging through a local mechanism as substantiated by ΔG_{HX} values less than 6 kcal·mol^{-1} and by guanidine independence of exchange (data not shown). The majority of residues (16, 21, 35, 37, 51, 52, 53, 54, 55, 56, 62, and 63) are significantly destabilized, some of which are listed above as exchanging through global unfolding. The resolution enabled by NMR provides site-specific reporters of conformational flexibility regardless of whether the exchange effects are local or global. These destabilized residues thus reveal increases in conformational flexibilities from local to global levels.

DISCUSSION

In this paper, the effect of the V54A mutation on the dynamics of eglin c has been expanded to include (i) picosecond to nanosecond motions of aromatic side chains, as determined from ^{13}C spin relaxation, and (ii) slower time scale motions probed by NMR-detected amide H/D exchange. The manner in which protein behavior changes in response to various perturbations (e.g., pH, ligand binding, mutation) is a central problem for understanding mechanisms of signal transmission. Perhaps the most fundamental type of transmission is the propagation of forces through a single protein domain (*3, 10, 12–14, 29, 52–55*). The V54A mutant may be considered to induce signal transmission, as this modest mutation affects the picosecond to nanosecond time scale motional fluctuations of side chains throughout the protein, as determined from methyl dynamics (*10*) (*15*). To obtain a more complete picture of the dynamic response, other side-chain types and slower time scales need to be considered, especially since many signal transmission effects occur on slower time scales, such as with allosteric conformational changes (*5, 11, 56–58*). Here, we show that model-free order parameters are readily obtained for aromatic groups using ^{13}C relaxation and that flexibility changes from hydrogen exchange measurements provide a view of the slower changes in dynamics in eglin c. Taking all data together, there is a striking spatial colocalization of compensating changes in fast and slow dynamics, suggesting a possible link between fast fluctuations and rare opening events.

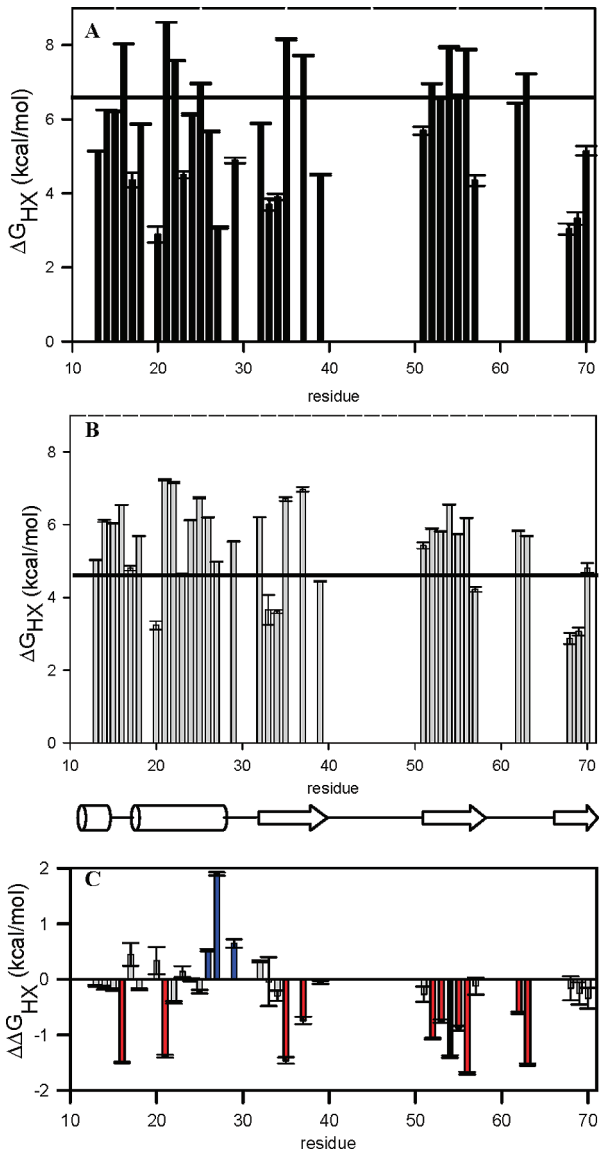

FIGURE 5: HX-determined local free energies and changes in local stabilities upon mutation. Shown here are the HX-determined local stabilities for WT (panel A) and V54A (panel B). The horizontal lines denote globally determined stability via fluorescence-monitored GdnHCl melts. The secondary structure of eglin is displayed beneath the lower panel. Differences in local stabilities (panel C) are shown as $\Delta\Delta G_{HX}$ (V54A − WT). Red bars indicate destabilization (increased rate of exchange), and blue bars indicate stabilization (slowed exchange). Black bars denotes the site of mutation.

Aromatic Picosecond to Nanosecond Dynamics from ^{13}C Relaxation. Here we find that application of canonical relaxation experiments (*37*) in concert with a new ^{13}C labeling scheme (*1*) yields high-quality information on the picosecond to nanosecond dynamics of 13 aromatic groups in eglin c. These data were evaluated by model selection (*59*), followed by model-specific fits to obtain model-free dynamics parameters. The final fits produced order parameters with average error less than 1.5%, highlighting the precision of these data; the corresponding χ^2 values are quite reasonable given the high precision and number of the relaxation experiments (six) analyzed. Aromatic S^2 and τ_e values show high variability, similar to methyl side-chain dynamics (*23*). Overall, aromatic S^2 values tend to be intermediate between backbone N−H (and C^α−H^α, as well as C^α−C′) S^2 values and methyl S^2_{axis} values. Perhaps most interesting, τ_e values tend to cluster around 1 ns (Figure 2B). Because this is observed for aromatic $\tau_{e/s}$ values derived from both model 2 and model 5, this appears not to result from model-specific bias. In addition, ~1 ns $\tau_{e/s}$ values were observed for bond vectors with both low and high order parameters. Given that rapid ring flipping alone yields a theoretical S^2 value of 0.44, these results suggest that the fast motions captured in the majority of aromatic S^2 values are not dominated by 180° ring flipping but rather are likely to arise from a variety of smaller torsional bond rotations. If rapid ring flips are a major contributor to the order parameter values (not including Y35 and Y49), this would require the inverses of the ring flip rates to be poised at or slightly longer than τ_m, which seems unlikely (see Results). To test the possibility that aromatic motions, and particularly ring flipping, occur on the microsecond to millisecond time scale, ^{13}C CPMG-relaxation dispersion experiments were also conducted; the dispersion curves observed were essentially flat (data not shown), indicating minimal motion on this time scale. Also, there is no evidence of line broadening in the aromatic spectrum. Therefore, it is reasonable to deduce that ring flipping is more likely occurring on the slow nanosecond to fast microsecond time scale for most aromatic residues in eglin c.

One simple way to understand order parameter values is to correlate them with packing, depth of burial, or solvent accessibility. For side chains, this has been primarily attempted with methyl S^2_{axis} parameters, which typically show at best a weak correlation (*23*). However, improvements have been achieved in some cases using additional parametrization (*60*). Because aromatic groups are observed both in the core and on the surface of eglin c, the correlation of aromatic S^2 values with solvent-accessible surface area (SASA) was examined, as it seemed possible that a stronger correlation might exist for aromatics vs methyl groups. Utilizing the web-based software GETAREA (*61*), we determined SASA for the aromatic side chains of WT and V54A [the latter modeled by RosettaDesign (*62*)]. A weak correlation is observed for aromatic residues, $R^2 = 0.39$, similar to $R^2 = 0.44$ for methyl side chains (data not shown).

A New Set of "Responders" to the V54A Perturbation. The previously published response to the V54A mutation showed a contiguous "network" of methyl-bearing residues that rigidified in response to mutation (*15*). With the addition of aromatic probes, the scope of the picosecond to nanosecond response is expanded, which now more completely agrees with the thermodynamic observations of Gribenko et al. (*16*). Specifically, the absence of significant heat capacity change (or change in entropy) may be explained by the increase in aromatic flexibility, which serves to offset the previously reported rigidification of methyl-containing side chains. It is possible that additional, yet-to-be-observed changes in side-chain dynamics (e.g., in hydrophilic side chains) may provide further damping of the methyl rigidification. Nevertheless, there still appears to be a slight overall rigidification of side-chain motions (Figure 4).

The overall dynamic response to V54A includes most of the hydrophobic core as one contiguous response network. By contrast, the reactive site loop appears to be unaffected. The rigidification now extends to Y32 and outward to the surface residues H65 and H68 (Figure 7). The cavity formed

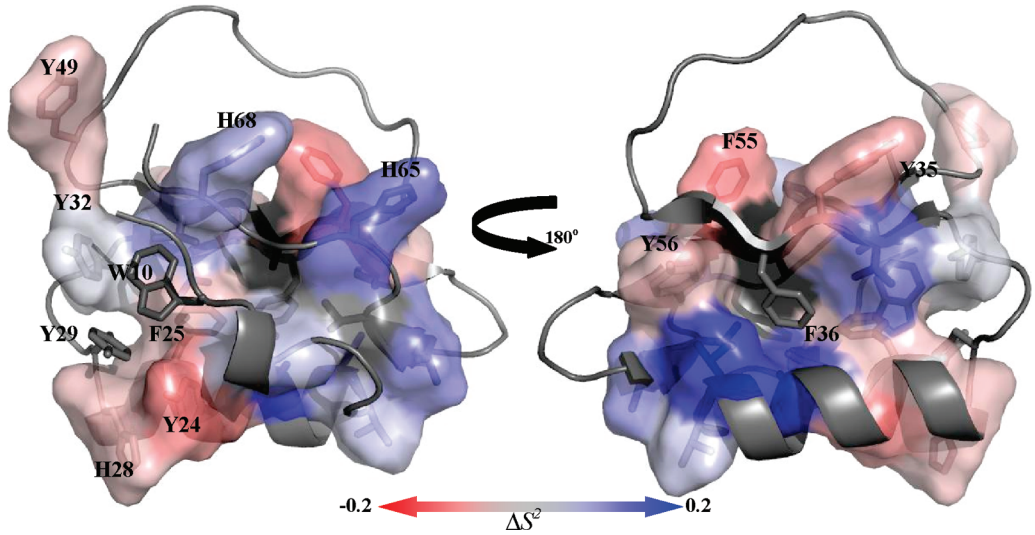

FIGURE 6: Picosecond to nanosecond dynamic network of methyl-bearing and aromatic side chains. The response of methyl-bearing and aromatic residues is shown on the structure of V54A eglin c. The level of response is denoted as a gradient from red (more flexible) to blue (more rigid). Aromatic residues are labeled with black letters. Gray sticks indicate residues with no significant response or residues with less reliable fits. Black denotes the site of the V54A mutation.

via mutation and the rigidification of neighboring residues seems to allow the gain of flexibility exhibited by F25, which packs into the core, and neighboring residues Y24 and H28. Aromatic residues sequentially adjacent to the mutation also display increased flexibility at F55 and Y56 with Y56 showing a significant change in τ_e. F35 and Y49 show increases in flexibility as well. Thus, the increase in aromatic flexibility laterally flanks the rigidification response. The V54A mutation may result in shifting of the balance of dynamic excursions between two complementary side chains.

Pocket of Stabilization/Rigidification in a Destabilized Mutant. Amide hydrogen exchange (HX) is often used as a measure of flexibility in proteins (*63, 64*). Both peripheral and core protein mutations have been shown to propagate responses to their counterparts [core to the periphery (*65*) and periphery to the core (*29*)]. This approach was taken to supplement the fast dynamic response with changes in slower motions. Under EX2 conditions, exchange rates may also be interpreted as local stabilities (*33, 66*). Changes in local stabilities probed here by hydrogen exchange are indeed supportive of dynamic signal transmission as reported by motions on a much slower time scale. Primarily, the core mutation V54A results in local destabilization throughout much of the protein, in agreement with reduced global stability. It should be mentioned, however, that some of these residues are not exchanging through a global mechanism (see Results), hence reflecting slow native state (or near native state) fluctuations. Remarkably, a cluster of residues incur a *stabilization* in a peripheral region of the protein 10–12 Å away from mutation (Figures 5 and 7). Such significant clustering of slowed exchange, in the opposite direction of global destabilization, has to our knowledge only been reported once before, in the protein Im7, upon mutating I72 to valine (*67*). That study attributed the increase in local stability (in the context of global destabilization) to a destabilization of a folding intermediate upon mutation; this essentially "traps" hydrogen-bonded groups by making an "open" state less accessible—a sort of rigidification. Destabilization of a folding intermediate seems less likely in the present analysis, as eglin c is a homologue of CI2, the archetype of two-state folding (*51*). Local stabilization is more likely to arise from (1) a compaction, or reduced number of states, in the continuum of lowly populated, locally unfolded states or (2) a decrease in frequency of fluctuations within the native state ensemble. Regardless of the mechanism, these residues (T26, L27, and Y29) are experiencing a slowing of exchange distal to the site of mutation, thus revealing energetic connectivity between the core residue (V54) and the peripheral responders consistent with an overall regional "rigidification".

Colocalization of Opposing Dynamic Responses on Different Time Scales. From the various dynamics/flexibility data now available on WT and V54A eglin c, we have observed a colocalization of opposing dynamic effects on different time scales. In what follows, the terms "flexibility" and "rigidification" will be used to describe the picosecond to nanosecond time scale, and local "stabilization" and "destabilization" (referring to local free energies) will be used to describe effects monitored by hydrogen exchange (and the slower motions implicit therein). The structural regions experiencing significant changes in fast and slow motions are highlighted on the structure of eglin c in Figure 7. Of particular note is that, in response to mutation, the regions of decreased stability and side-chain flexibility map to the same locale (Figure 7A). Moreover, the converse is largely true: the region that becomes (curiously) significantly stabilized coincides with an increase in side-chain flexibility (Figure 7B).

To more rigorously test the idea that opposing dynamic effects on different time scales colocalize, we constructed a two-way contingency table (Table 2) and used a Fisher exact test (*44, 45*) to test for correlation. The null hypothesis is that these multi-time scale dynamic events are strictly independent, the alternative hypothesis being that the events are in some way related. The contingency table categorizes residues according to changes in stability (rows) and flexibility (columns). For amides that showed significant stabi-

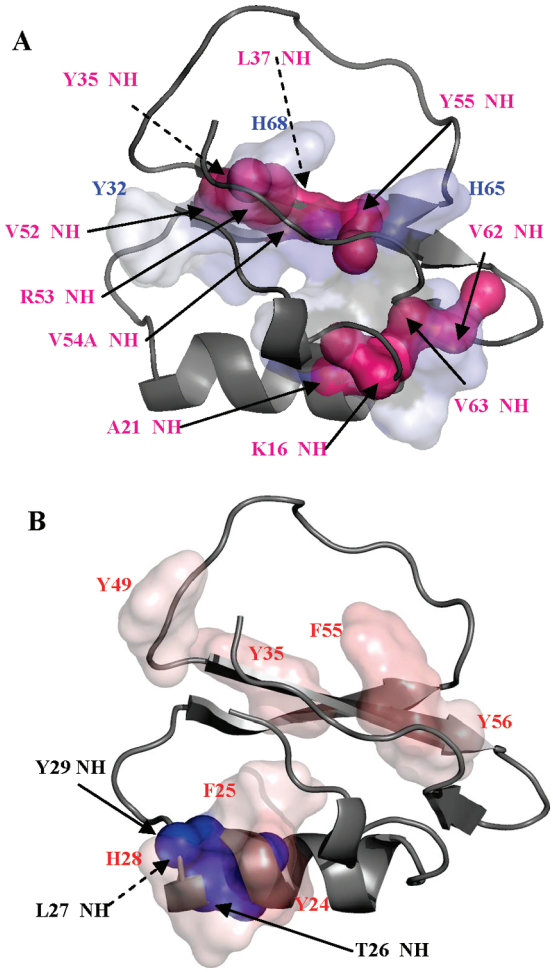

FIGURE 7: Colocalization of significant motional changes on different time scales. (A) Residues that display a significant increase in rigidity on the picosecond to nanosecond time scale are shown as a contiguous van der Waals surface in slate. V63, an inferred member of the network, is shown in gray. Aromatic reporters are labeled in blue letters. Individual magenta surfaces represent amide nitrogens and carbonyl oxygens that participate in hydrogen bonds in regions where significant decreases ($\Delta\Delta G_{HX} < -0.5$ kcal·mol^{-1}) in local stability are observed. The corresponding nitrogens are labeled in magenta letters as well. Dotted arrows indicate that the labeled entity is located in the back of the structure as arranged. (B) Residues that display significant increase in flexibility on the picosecond to nanosecond time scale are shown as two regions of contiguous van der Waals surfaces in red. Aromatic reporters are labeled in red letters. Individual blue surfaces represent amide nitrogens and carbonyl oxygens that participate in hydrogen bonds in regions where significant increases ($\Delta\Delta G_{HX} > 0.5$ kcal·mol^{-1}) in local stability are observed. The corresponding nitrogens are labeled in black letters.

lization (or destabilization), any residues with heavy atoms within 3 Å (approximate N-to-O distance in a hydrogen bond) of either the amide nitrogen or corresponding oxygen (hydrogen bond acceptor) were categorized according to their side-chain flexibility response: more flexible, more rigid, or no change. There are two regions of destabilization and one region of stabilization upon the V54A mutation (Figure 7). In essence, each entry in the contingency table reflects the flexibility of a side chain that is in or adjacent to a given region of stability change. Only "reporting" residues for which order parameters were available for both wild type and mutant were considered. For example, of the residues that gained stability upon mutation, three nearby side chains became more flexible and one nearby side chain showed no change. The resultant contingency table is shown in Table 2, with the observed number of residues for each category. The values in parentheses were determined assuming the null hypothesis (that changes in stability and flexibility are independent) is true. Because the number of entries in the table are small, a Fisher exact test (see Experimental Procedures) was used to calculate the *p*-value, determined to be 0.0246. Thus the null hypothesis is rejected in favor of the alternative hypothesis that stabilization (destabilization) colocalizes with increases (decreases) in flexibility, in response to V54A mutation in eglin c.

Table 2: Contingency Table Showing Colocalization of Picosecond to Nanosecond Flexibility and Local Stability[a]

	more flexible	more rigid	no change	total
stabilized[b]	3 (1.09)	0 (2.00)	1 (0.91)	4
destabilized[c]	3 (4.91)	11 (9.00)	4 (4.09)	18
total	6	11	5	22

[a] Numbers in the table are observed occurrences. Numbers in parentheses are expected occurrences calculated assuming independence between phenomena. In instances where the expected values are small, a Fisher exact test is more robust in determining a *p*-value (*44, 45*). The Fisher exact test gives a *p*-value of 0.0246 and a rejection of the null hypothesis, finding that these occurrences are indeed correlated. [b] Considered a significant stabilization if $\Delta\Delta G_{HX}$ is greater than 0.5 kcal·mol^{-1}. [c] Considered a significant destabilization if $\Delta\Delta G_{HX}$ is less than –0.5 kcal·mol^{-1}.

Recently, it has been shown in the protein calmodulin that changes in order parameters have a linear relationship with conformational entropy upon binding (*68*). The colocalization of opposing changes in local stability (slow dynamics) and changes in order parameters (fast dynamics) seen here suggests the possibility of a similar conformational entropy term contributing to local free energies measured by native hydrogen exchange. This assumes a negligible change in local enthalpic contributions (minimal structural perturbation) for this mutant, which is the case for the V54A mutant (*15*). Viewed somewhat differently, the colocalization can be seen as evidence for linkage between fast and slow motions. Whether this is entropy-driven or arises through other mechanisms is not presently clear. Future experiments should bear out whether the colocalization observed here is generally true for eglin c or unique to the V54A mutation. Interestingly, an anticorrelated relationship between global stability and local rigidity was previously observed in pH studies of eglin c (*69*).

CONCLUSION

The fast (picosecond to nanosecond) dynamic response of eglin c to the centrally located V54A mutation has been expanded to include aromatic S^2 and $\tau_{e/s}$ values obtained from ^{13}C relaxation, which was made highly convenient based on the ^{13}C labeling scheme of Teilum et al. (*1*). The fast dynamic response appears to fill out the majority of the globular region of the protein, but not the reactive site loop, consistent with long-range perturbation based on the conservative, local perturbation. To address slower events, amide hydrogen exchange was used to determine local residue stabilities. Surprisingly, even though the V54A mutant is globally destabilized by 1.5 kcal·mol^{-1}, a pocket of residues showed increases in stability of up to 2 kcal·mol^{-1}. This pocket colocalizes with a region of increased aromatic flexibility.

The general observation of colocalization of opposite dynamic effects on fast and slow time scales points to a possible relationship between fast dynamic fluctuations and relatively rare structural perturbations that lead to hydrogen exchange. This analysis was made possible only after use of additional probes of motion on different time scales.

ACKNOWLEDGMENT

The authors thank Yaiwen Bai for helpful discussions on hydrogen exchange and Michael W. Clarkson for assignments used in this study. We also acknowledge the Macromolecular Interactions Facility, The Pharmacy NMR Facility, and the Biomolecular NMR Laboratory of the University of North Carolina.

REFERENCES

1. Teilum, K., Brath, U., Lundstrom, P., and Akke, M. (2006) Biosynthetic ^{13}C labeling of aromatic side chains in proteins for NMR relaxation measurements. *J. Am. Chem. Soc. 128*, 2506–2507.
2. Boehr, D. D., McElheny, D., Dyson, H. J., and Wright, P. E. (2006) The dynamic energy landscape of dihydrofolate reductase catalysis. *Science 313*, 1638–1642.
3. Formaneck, M. S., Ma, L., and Cui, Q. (2006) Reconciling the "old" and "new" views of protein allostery: A molecular simulation study of chemotaxis Y protein (chey). *Proteins: Struct., Funct., Bioinf. 63*, 846–867.
4. Karplus, M., and Kuriyan, J. (2005) Molecular dynamics and protein function. *Proc. Natl. Acad. Sci. U.S.A. 102*, 6679–6685.
5. Kern, D., and Zuiderweg, E. R. P. (2003) The role of dynamics in allosteric regulation. *Curr. Opin. Struct. Biol. 13*, 748–757.
6. Wand, A. J. (2001) Dynamic activation of protein function: A view emerging from NMR spectroscopy. *Nat. Struct. Biol. 8*, 926–931.
7. Liu, T., Whitten, S. T., and Hilser, V. J. (2007) Functional residues serve a dominant role in mediating the cooperativity of the protein ensemble. *Proc. Natl. Acad. Sci. U.S.A. 104*, 4347–4352.
8. Pezza, J. A., Stopa, J. D., Brunyak, E. M., Allen, K. N., and Tolan, D. R. (2007) Thermodynamic analysis shows conformational coupling and dynamics confer substrate specificity in fructose-1,6-bisphosphate aldolase. *Biochemistry 46*, 13010–13018.
9. Sharp, K., and Skinner, J. J. (2006) Pump-probe molecular dynamics as a tool for studying protein motion and long range coupling. *Proteins: Struct., Funct., Bioinf. 65*, 347–361.
10. Clarkson, M. W., Gilmore, S. A., Edgell, M. H., and Lee, A. L. (2006) Dynamic coupling and allosteric behavior in a nonallosteric protein. *Biochemistry 45*, 7693–7699.
11. Popovych, N., Sun, S., Ebright, R. H., and Kalodimos, C. G. (2006) Dynamically driven protein allostery. *Nat. Struct. Mol. Biol. 13*, 831–838.
12. Ota, N., and Agard, D. A. (2005) Intramolecular signaling pathways revealed by modeling anisotropic thermal diffusion. *J. Mol. Biol. 351*, 345–354.
13. Fuentes, E. J., Der, C. J., and Lee, A. L. (2004) Ligand-dependent dynamics and intramolecular signaling in a PDZ domain. *J. Mol. Biol. 335*, 1105–1115.
14. Pan, H., Lee, J. C., and Hilser, V. J. (2000) Binding sites in *Escherichia coli* dihydrofolate reductase communicate by modulating the conformational ensemble. *Proc. Natl. Acad. Sci. U.S.A. 97*, 12020–12025.
15. Clarkson, M. W., and Lee, A. L. (2004) Long-range dynamic effects of point mutations propagate through side chains in the serine protease inhibitor eglin c. *Biochemistry 43*, 12448–12458.
16. Gribenko, A. V., Keiffer, T. R., and Makhatadze, G. I. (2006) Amino acid substitutions affecting protein dynamics in eglin c do not affect heat capacity change upon unfolding. *Proteins: Struct., Funct., Bioinf. 64*, 295–300.
17. Koide, A., Gilbreth, R. N., Esaki, K., Tereshko, V., and Koide, S. (2007) High-affinity single-domain binding proteins with a binary-code interface. *Proc. Natl. Acad. Sci. U.S.A. 104*, 6632–6637.
18. Fellouse, F. A., Wiesmann, C., and Sidhu, S. S. (2004) Synthetic antibodies from a four-amino-acid code: A dominant role for tyrosine in antigen recognition. *Proc. Natl. Acad. Sci. U.S.A. 101*, 12467–12472.
19. Lo Conte, L., Chothia, C., and Janin, J. (1999) The atomic structure of protein-protein recognition sites. *J. Mol. Biol. 285*, 2177–2198.
20. Bogan, A. A., and Thorn, K. S. (1998) Anatomy of hot spots in protein interfaces. *J. Mol. Biol. 280*, 1–9.
21. Palmer, A. G., Hochstrasser, R. A., Millar, D. P., Rance, M., and Wright, P. E. (1993) Characterization of amino acid side chain dynamics in a zinc-finger peptide using ^{13}C NMR spectroscopy and time-resolved flourescence spectroscopy. *J. Am. Chem. Soc. 115*, 6333–6345.
22. LeMaster, D. M., and Kushlan, D. M. (1996) Dynamical mapping of *E. coli* thioredoxin via ^{13}C NMR relaxation analysis. *J. Am. Chem. Soc. 118*, 9255–9264.
23. Igumenova, T. I., Frederick, K. K., and Wand, A. J. (2006) Characterization of the fast dynamics of protein amino acid side chains using NMR relaxation in solution. *Chem. Rev. 106*, 1672–1699.
24. Lipari, G., and Szabo, A. (1982) Model-free approach to the interpretation of nuclear magnetic resonance relaxation in macromolecules. 1. Theory and range of validity. *J. Am. Chem. Soc. 104*, 4546–4559.
25. Lipari, G., and Szabo, A. (1982) Model-free approach to the interpretation of nuclear magnetic resonance relaxation in macromolecules. 2. Analysis of experimental results. *J. Am. Chem. Soc. 104*, 4559–4570.
26. Casares, S., Lopez-Mayorga, O., Vega, S., Camara-Artigas, A., and Conejero-Lara, F. (2007) Cooperative propagation of local stability changes from low-stability and high-stability regions in a SH3 domain. *Proteins: Struct., Funct., Bioinf. 67*, 531–547.
27. Fuentes, E. J., Gilmore, S. A., Mauldin, R. V., and Lee, A. L. (2006) Evaluation of energetic and dynamic coupling networks in a PDZ domain protein. *J. Mol. Biol. 364*, 337–351.
28. Casares, S., Sadqi, M., Lopez-Mayorga, O., Martinez, J. C., and Conejero-Lara, F. (2003) Structural cooperativity in the SH3 domain studied by site-directed mutagenesis and amide hydrogen exchange. *FEBS Lett. 539*, 125–130.
29. Spudich, G., Lorenz, S., and Marqusee, S. (2002) Propagation of a single destabilizing mutation throughout the *Escherichia coli* ribonuclease HI native state. *Protein Sci. 11*, 522–528.
30. De-Lorimier, R., Hellinga, H. W., and Spicer, L. D. (1996) NMR studies of structure, hydrogen exchange, and main-chain dynamics in a disrupted-core mutant of thioredoxin. *Protein Sci. 5*, 2552–2565.
31. Englander, S. W., and Kallenbach, N. R. (1983) Hydrogen-exchange and structural dynamics of proteins and nucleic-acids. *Q. Rev. Biophys. 16*, 521–655.
32. Bai, Y. W., Milne, J. S., Mayne, L., and Englander, S. W. (1993) Primary structure effects on peptide group hydrogen-exchange. *Proteins 17*, 75–86.
33. Bai, Y. W., Milne, J. S., Mayne, L., and Englander, S. W. (1994) Protein stability parameters measured by hydrogen-exchange. *Proteins 20*, 4–14.
34. Delaglio, F., Grzesiek, S., Vuister, G. W., Zhu, G., Pfeifer, J., and Bax, A. (1995) NMRPipe—a multidimensional spectral processing system based on Unix pipes. *J. Biomol. NMR 6*, 277–293.
35. Johnson, B. A., and Blevins, R. A. (1994) Nmrview: A computer program for the visualization and analysis of NMR data. *J. Biomol. NMR 4*, 603–614.
36. Yamazaki, T., Formankay, J. D., and Kay, L. E. (1993) 2-Dimensional NMR experiments for correlating ^{13}C-beta and ^{1}H-delta/epsilon chemical-shifts of aromatic residues in ^{13}C-labeled proteins via scalar couplings. *J. Am. Chem. Soc. 115*, 11054–11055.
37. Farrow, N. A., Muhandiram, R., Singer, A. U., Pascal, S. M., Kay, C. M., Gish, G., Shoelson, S. E., Pawson, T., Forman-Kay, J. D., and Kay, L. E. (1994) Backbone dynamics of a free and phosphopeptide-complexed Src homology 2 domain studied by ^{15}N NMR relaxation. *Biochemistry 33*, 5984–6003.
38. Bremi, T., Ernst, M., and Ernst, R. R. (1994) Side-chain motion with two degrees of freedom in peptides. An NMR study of phenylalanine side chains in antamanide. *J. Phys. Chem. 98*, 9322–9334.
39. Stone, M. J., Chandrasekhar, K., Holmgren, A., Wright, P. E., and Dyson, H. J. (1993) Comparison of backbone and tryptophan side-chain dynamics of reduced and oxidized *Escherichia coli* thioredoxin using ^{15}N NMR relaxation measurements. *Biochemistry 32*, 426–435.
40. d'Auvergne, E. J., and Gooley, P. R. (2003) The use of model selection in the model-free analysis of protein dynamics. *J. Biomol. NMR 25*, 25–39.

41. Schanda, P., and Brutscher, B. (2005) Very fast two-dimensional NMR spectroscopy for real-time investigation of dynamic events om proteins on the time scale of seconds. *J. Am. Chem. Soc. 127*, 8014–8015.
42. Edgell, M. H., Sims, D. A., Pielak, G. J., and Yi, F. (2003) High-precision, high-throughput stability determinations facilitated by robotics and a semiautomated titrating fluorometer. *Biochemistry 42*, 7587–7593.
43. Jackson, S. E., and Fersht, A. R. (1991) Folding of chymotrypsin inhibitor 2. Evidence for a two-state transtion. *Biochemistry 30*, 10428–10435.
44. Applegate, K. E., Tello, R., and Ying, J. (2003) Hypothesis testing III: Counts and medians. *Radiology 228*, 603–608.
45. Fisher, R. A. (1935) The logic of inductive inference. *J. R. Stat. Soc. 98*, 39–82.
46. Jacob, J., Louis, J. M., Nesheiwat, I., and Torchia, D. A. (2002) Biosynthetically directed fractional ^{13}C labeling facilitates identification of Phe and Tyr aromatic signals in proteins. *J. Biomol. NMR 24*, 231–235.
47. Hu, H., Hermans, J., and Lee, A. L. (2005) Relating side-chain mobility in proteins to rotameric transitions: Insights from molecular dynamics simulations and NMR. *J. Biomol. NMR 32*, 151–162.
48. Vugmeyster, L., Raleigh, D. P., Palmer, A. G., III, and Vugmeister, B. E. (2003) Beyond the decoupling approximation in the model-free approach for the interpretation of NMR relaxation of macromolecules in solution. *J. Am. Chem. Soc. 125*, 8400–8404.
49. Liang, X.,., Lee, G.-i., and Van Doren, S. R. (2006) Partially unfolded forms and non-two-state folding of a β-sandwich: FHA domain from arabidopsis receptor kinase-associated protein phosphatase. *J. Mol. Biol. 364*, 225–240.
50. Ohnishi, S., Lee, A. L., Edgell, M. H., and Shortle, D. (2004) Direct demonstration of structural similarity between native and denatured eglin c. *Biochemistry 43*, 4064–4070.
51. Neira, J. L., Itzhaki, L. S., Otzen, D. E., Davis, B., and Fersht, A. R. (1997) Hydrogen exchange in chymotrypsin inhibitor 2 probed by mutagenesis. *J. Mol. Biol. 270*, 99–110.
52. Swain, J. F., and Gierasch, L. M. (2006) The changing landscape of protein allostery. *Curr. Opin. Struct. Biol. 16*, 102–108.
53. Baysal, C., and Atilgan, A. R. (2001) Coordination topology and stability for the native and binding conformers of chymotrypsin inhibitor 2. *Proteins 45*, 62–70.
54. Hilser, V. J., Dowdy, D., Oas, T. G., and Freire, E. (1998) The structural distribution of cooperative interactions in proteins: Analysis of the native state ensemble. *Proc. Natl. Acad. Sci. U.S.A. 95*, 9903–9908.
55. Cooper, A., and Dryden, D. T. F. (1984) Allostery without conformational change—a plausible model. *Eur. Biophys. J. Biophys. Lett. 11*, 103–109.
56. Zhou, H., Shatz, W., Purdy, M. M., Fera, N., Dahlquist, F. W., and Reich, N. O. (2007) Long-range structural and dynamical changes induced by cofactor binding in DNA methyltransferase m.Hhai. *Biochemistry 46*, 7261–7268.
57. Rist, W., Graf, C., Bukau, B., and Mayer, M. P. (2006) Amide hydrogen exchange reveals conformational changes in hsp70 chaperones important for allosteric regulation. *J. Biol. Chem. 281*, 16493–16501.
58. Andersen, M. D., Shaffer, J., Jennings, P. A., and Adams, J. A. (2001) Structural characterization of protein kinase A as a function of nucleotide binding: Hydrogen-deuterium exchange studies using MALDI-TOF MS detection. *J. Biol. Chem.* 14204–14211.
59. Mandel, A. M., Akke, M., and Palmer, A. G. (1995) Backbone dynamic of *Escherichia coli* ribonuclease HI: Correlations with structure and function in an active enzyme. *J. Mol. Biol. 246*, 144–163.
60. Ming, D., and Bruschweiler, R. (2004) Prediction of methyl-side chain dynamics in proteins. *J. Biomol. NMR 29*, 363–368.
61. Fraczkiewicz, R., and Braun, W. (1998) Exact and efficient analytical calculation of the accessible surface areas and their gradients for macromolecules. *J. Comput. Chem. 19*, 319–333.
62. Liu, Y., and Kuhlman, B. (2006) RosettaDesign server for protein design. *Nucleic Acids Res. 34*, 238.
63. Hernandez, G., Jenney, F. E., Jr., Adams, M. W., and LeMaster, D. M. (2000) Millisecond time scale conformational flexibility in a hyperthermophile protein at ambient temperature. *Proc. Natl. Acad. Sci. U.S.A. 97*, 3166–3170.
64. Polshakov, V. I., Birdsall, B., and Feeney, J. (2006) Effects of co-operative ligand binding on protein amide NH hydrogen exchange. *J. Mol. Biol. 356*, 886–903.
65. Xu, J., Baase, W. A., Baldwin, E., and Matthews, B. W. (1998) The response of T4 lysozyme to large-to-small substitutions within the core and its relation to the hydrophobic effect. *Protein Sci. 7*, 158–177.
66. Hilser, V. J., and Freire, E. (1996) Structure-based calculation of the equilibrium folding pathway of proteins. Correlation with hydrogen exchange protection factors. *J. Mol. Biol. 262*, 756–772.
67. Gorski, S. A., Le Duff, C. S., Capaldi, A. P., Kalverda, A. P., Beddard, G. S., Moore, G. R., and Radford, S. E. (2004) Equilibrium hydrogen exchange reveals extensive hydrogen bonded secondary structure in the on-pathway intermediate of Im7. *J. Mol. Biol. 337*, 183–193.
68. Frederick, K. K., Marlow, M. S., Valentine, K. G., and Wand, A. J. (2007) Conformational entropy in molecular recognition by proteins. *Nature 448*, 325–329.
69. Hu, H., Clarkson, M. W., Hermans, J., and Lee, A. L. (2003) Increased rigidity of eglin c at acidic pH: Evidence from NMR spin relaxation and MD simulations. *Biochemistry 42*, 13856–13868.
70. Bode, W., Papamokos, E., and Musil, D. (1987) The high-resolution X-ray crystal structure of the complex formed between subtilisin Carlsberg and eglin c, an elastase inhibitor from the leech *Hirudo medicinalis*. Structural analysis, subtilisin structure and interface geometry. *Eur. J. Biochem. 166*, 673–692.

BI702330T